Oxygen Reduction

DOI: 10.1002/ange.201209548

# Two-Step Boron and Nitrogen Doping in Graphene for Enhanced Synergistic Catalysis**

*Yao Zheng, Yan Jiao, Lei Ge, Mietek Jaroniec, and Shi Zhang Qiao**

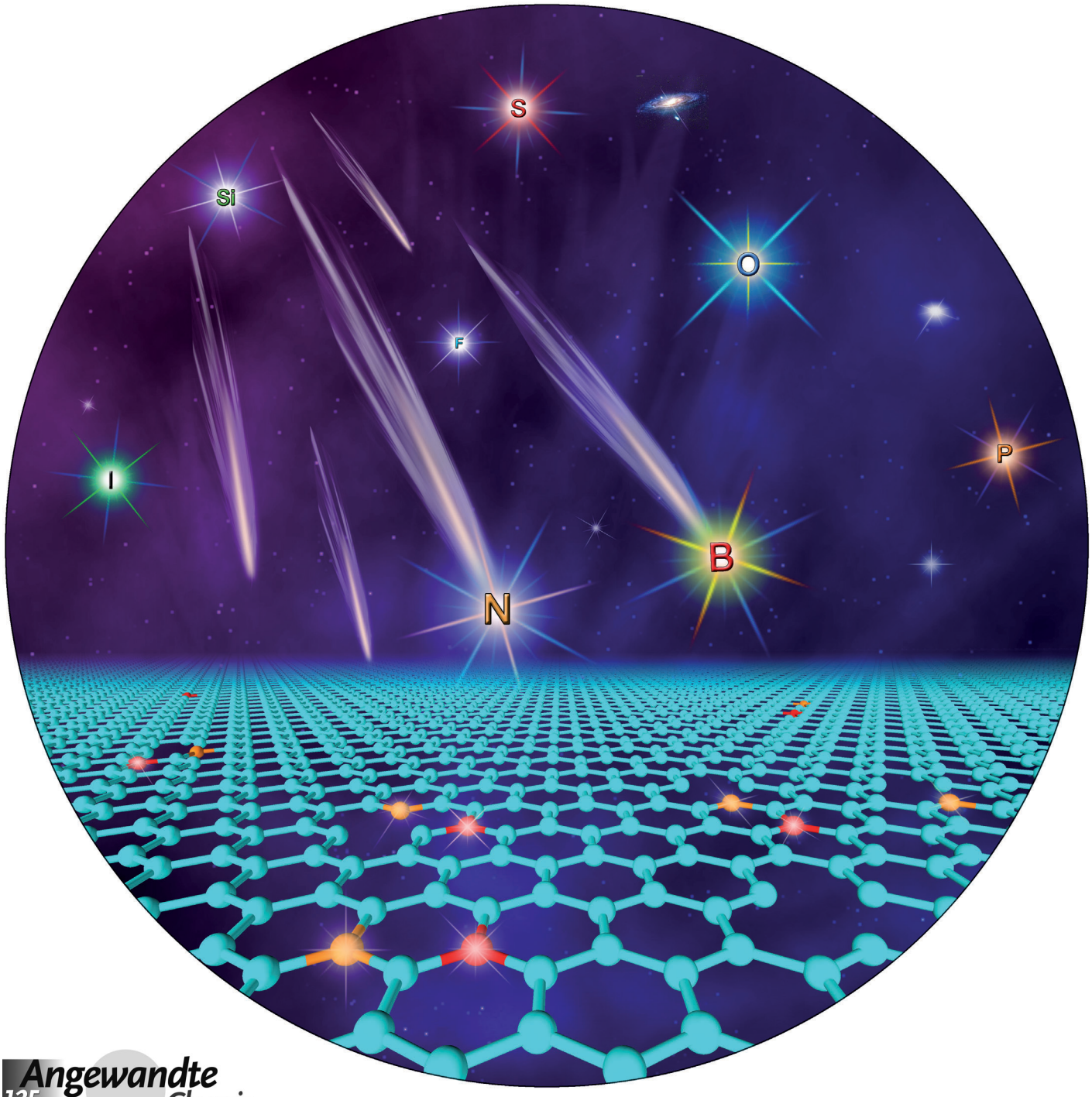

The replacement of high-cost and scarce precious-metal catalysts with commercially available alternatives has attracted much attention from both industrial and academic researchers in catalysis. Although extensive studies have been conducted in the search for non-precious-metal catalysts, the results are far from satisfactory owing to the limited performance of the discovered catalysts and environmental hazards. Meanwhile, both theoretical calculations and experiments have demonstrated the considerable activity of cost-effective metal-free materials with unique electronic and nanostructural properties in a wide range of heterogeneous, electrochemical, and photocatalytic processes.[1] A particularly exciting example was the development of nitrogen-doped carbon materials, which revealed competitive activity and significantly enhanced stability as compared to commercial Pt/C catalysts in the critical but sluggish oxygen reduction reaction (ORR) in fuel cells and metal–air batteries.[1c,2] These promising features have generated interest in the development of nanostructured metal-free catalysts with analogous functions and comparable reactivity to those of conventional noble metals.

Current state-of-the-art metal-free catalysts are $sp^2$-hybridized carbon and its derivatives, which are semimetals with a small number of metallic electrons at the surface.[1a] Graphene, as the mother of all carbon allotropes, provides an effective platform for fundamental investigations of the nature of metal-like reactivity in all carbon-based materials. For catalytic applications, the engineering of pristine graphene by the substitution of some carbon atoms with heteroatoms, such as N, B, P, I and S, is an effective way to tailor its electron-donor properties and consequently to enhance its catalytic activity.[3] In particular, codoping with two elements, one with higher and one with lower electronegativity than that of C ($\chi = 2.55$), for example, B ($\chi = 2.04$) and N ($\chi = 3.04$), can create a unique electronic structure with a synergistic coupling effect between heteroatoms. This effect makes such dual-doped graphene catalysts much more catalytically active than singly doped graphene catalysts.[4] In this regard, the codoping of graphene with two or more selected heteroatoms is becoming one of the main trends in the tailoring of its chemical and physical properties for desired applications.[4,5]

However, current approaches based on thermal chemical vapor deposition (CVD) for the synthesis of dual-doped graphene are too tedious and expensive for mass production.[4a,6] Although a recently reported chemical method involving the coannealing of solution-exfoliated graphene oxide in the presence of boric acid and ammonia is facile,[4b] it produced a covalent boron–carbon–nitride (BCN) but not a B- and N-codoped graphene (B,N-graphene). Moreover, almost all physical and chemical strategies inevitably lead to undesired by-products, such as hexagonal boron nitride (*h*-BN), which is chemically inert and results in poor activity of the catalyst. Despite tremendous progress in the synthesis of ternary BCN heteroring nanomaterials,[7] a high-phase-purity B,N-graphene in which B and N replace C atoms in the graphene framework at well-defined doping sites has not been reported, which makes the theoretical identification of the function of guest dopants impossible. Therefore, the nature of proposed synergistic effects remains inconclusive.

In this study, a *h*-BN-free B,N-graphene was prepared by a two-step doping method. This new method not only enables the incorporation of heteroatoms at selected sites of the graphene framework to induce a synergistic enhancement of the activity of the B,N-graphene, but it also prevents the formation of inactive by-products. The new catalyst shows excellent activity in the ORR and perfect (nearly 100%) selectivity for the four-electron ORR pathway in an alkaline medium. Its activity and four-electron pathway selectivity in the ORR is much higher than that observed for singly B- or N-doped graphenes. The B,N-graphene also shows complete methanol tolerance and excellent long-term stability; these properties are superior to those observed for the commercial Pt/C catalyst. The newly identified B–C–N configuration at the same time provides a platform for theoretical investigation of the nature of this significant enhancement in electrochemical performance. Density functional theory (DFT) calculations indicated that the chemical coupling of B and N is the origin of a synergistic effect that boosts the ORR activity of the B,N-graphene through an alternative mechanism to that observed for singly doped graphene with B or N. Furthermore, the role of each heteroatom in this synergistic catalysis was clarified fundamentally on the level of molecular orbitals. The current study of the ORR on B,N-graphene may provide new insight into the molecular design and feasible synthesis of more advanced graphene-based catalysts for potential applications in fuel cells and metal–air batteries.

B,N-graphene was synthesized from solution-exfoliated graphene oxide (GO) by a two-step doping strategy: first, N was incorporated by annealing with $NH_3$ at an intermediate temperature (e.g. 500 °C), and then B was introduced by pyrolysis of the intermediate material (N-graphene) with $H_3BO_3$ at a higher temperature (e.g. 900 °C; see the Supporting Information for the detailed procedure). The nanosheet morphology was preserved after the two-step doping procedure, as shown by transmission electron microscopy (TEM) and scanning electron microscopy (SEM; Figure 1; see also Figure S2 in the Supporting Information). At the same time, the electron energy loss spectrum (EELS) and elemental

[*] Y. Zheng, Dr. Y. Jiao, Prof. S. Z. Qiao
School of Chemical Engineering
The University of Adelaide, Adelaide, SA 5005 (Australia)
E-mail: s.qiao@adelaide.edu.au
Y. Zheng, Dr. Y. Jiao
Australian Institute for Bioengineering and Nanotechnology
University of Queensland, Brisbane, QLD 4072 (Australia)
L. Ge
School of Chemical Engineering
University of Queensland, Brisbane, QLD 4072 (Australia)
Prof. M. Jaroniec
Department of Chemistry and Biochemistry
Kent State University, Kent, Ohio 44242 (USA)

[**] This research was supported financially by the Australian Research Council (ARC) through the Discovery Project program (DP1095861, DP0987969).

Supporting information for this article is available on the WWW under http://dx.doi.org/10.1002/anie.201209548.

  

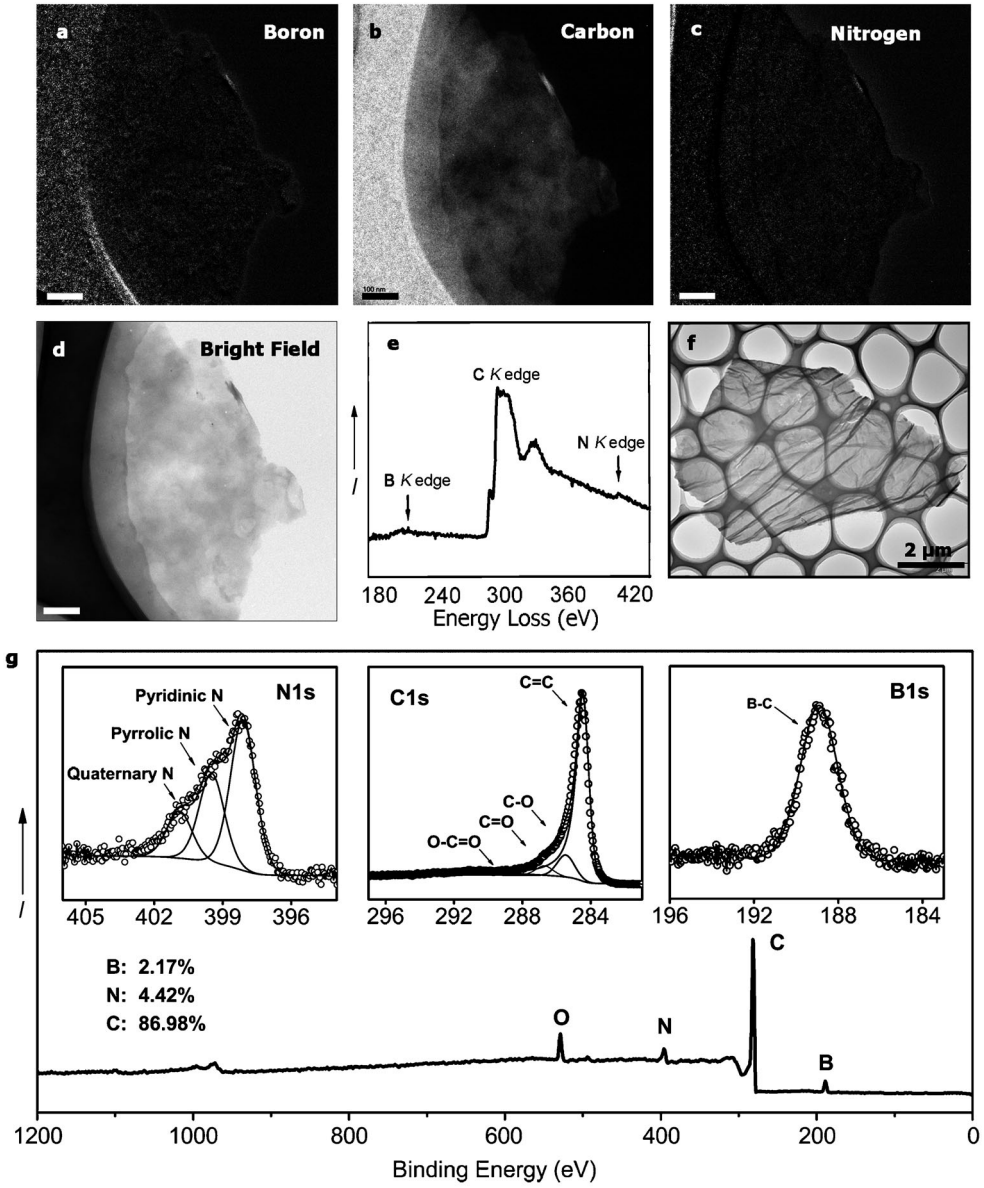


***Figure 1.*** a–d) Elemental mapping and e) EELS spectrum of B,N-graphene (the scale bar is 100 nm). f) Low-magnification TEM image of B,N-graphene. g) XPS survey and high-resolution spectra of N, C, and B 1s core levels in B,N-graphene.

mapping confirmed the coexistence of B and N in the graphene matrix in a homogeneous distribution (Figure 1 a–e).

The nature of doping was identified by X-ray photoelectron spectroscopy (XPS) with peak deconvolution (Figure 1 g). The analysis showed that conventional one-step doping (i.e. the simultaneous introduction of B and N heteroatoms) results in a low yield of B,N-graphene with a large amount of the by-product *h*-BN with the formation of a *h*-BN/graphene hybrid as the final product (see Figure S1 and Tables S1 and S2 in the Supporting Information). In contrast, through the newly developed sequential incorporation of the heteroatoms, all N heteroatoms in the resulting B,N-graphene are bonded to the surrounding C atoms in pyridinic N (ca. 2.03 atom %, BE (binding energy) = 398.3 eV[8]), pyrrolic N (ca. 1.29 atom %, BE = 400.3 eV[8]), and graphitic N forms (ca. 0.90 atom %, BE = 401.1 eV[8]; Figure 1 g), without any N–B configuration (BE = 397.9 eV[6a]). The ratios of these N species in the final B,N-graphene are close to those in the intermediate N-graphene (see Figure S2a), which further indicates that N species are preserved during the second doping process with B. Additionally, the symmetrical peak in the high-resolution B 1s spectrum (Figure 1 g) indicates that all B heteroatoms are bonded to C atoms only in the form of a $BC_3$ structure (ca. 2.17 atom %, BE = 188.9 eV[3d]), but not coupled with N (BE = 190.1 eV[4b]). This $BC_3$ bonding type indicates that all B heteroatoms have replaced C atoms in the framework of graphene without the formation of the undesired *h*-BN hybrid. It was also found that a reversed doping sequence, that is, first with B and then with N, can result in a low N content (overall ca. 1.55 atom %; see Table S2) and alternative B bonding types (coexistence of $BC_3$ and $BC_2O$, which may form in the first step as a result of the large amount of active oxygen in GO). With the normal doping sequence and the same second-step doping procedure (e.g. 900 °C for B incorporation), a higher annealing temperature in the first step (e.g. 900 °C for N incorporation) can also reduce the heteroatom content in the final product (not shown herein).

The typical Fourier transform IR (FTIR) spectra (Figure 2 a) also suggest that B and N were each coupled to C without a *h*-BN phase in B,N-graphene. In contrast, the IR adsorption bands characteristic for *h*-BN or ternary BCN were observed in the case of the *h*-BN/graphene hybrid obtained in the one-step synthesis; the main peak centered at approximately 1350 $cm^{-1}$ corresponds to the in-plane stretching vibrations within the fused BCN heterorings, and the minor absorption band at 710–830 $cm^{-1}$ is ascribed to the corresponding out-of-plane bending modes.[6d] In the Raman

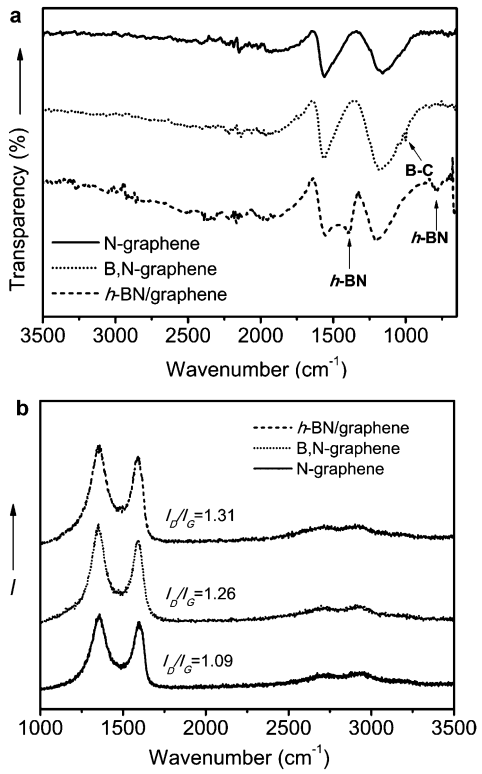


***Figure 2.*** a) FTIR and b) Raman spectra of N-graphene, B,N-graphene, and *h*-BN/graphene (synthesized in one step).

spectra (Figure 2b), there are nonobvious shifts of the D and G bands located at 1360 and 1590 $cm^{-1}$, respectively. The $I_D/I_G$ intensity ratio, which relates to a series of defects, increases from N-graphene to B,N-graphene. This increase can be attributed to the different C–C and C–N/C–B bond distances and provides further evidence for the existence of B and N in the graphene domains. *h*-BN/graphene shows a wider D band and higher $I_D/I_G$ ratio than B,N-graphene as a result of the large amount of hybrid *h*-BN in the composite; these features support the aforementioned XPS and FTIR results.

The electrocatalytic oxygen reduction was used as a probe reaction to assess the synergistically enhanced activity of B,N-graphene. The influence of single/double dopants on the ORR activity of various electrodes was first evaluated by cyclic voltammetry (CV) in an $O_2$-saturated 0.1 M solution of KOH. Pristine GO showed negligible ORR activity: the two separate oxygen-reduction peaks observed in the testing range of CV (see Figure S4a) indicate a weak and inefficient two-electron ORR process. Single B or N doping can significantly boost the activity of GO by generating additional active sites (see Figure S4b,c); the performances of single-element-doped catalysts can be further enhanced by the incorporation of a second heteroatom (see Figure S4d). Of the dual-doped catalysts, B,N-graphene showed a higher cathodic current density, which indicates more efficient ORR performance, than that observed for the *h*-BN/graphene hybrid (Figure 3a). A series of linear sweep voltammograms (LSVs) collected on a rotating disk electrode (RDE) further revealed that B,N-graphene has an onset potential closer to that of Pt/C than to that of home-made B- or N-graphene electrodes (see Figure S5 and Table S3); the more positive onset potential of B,N-graphene indicates a more facile ORR process. Additionally, the ORR current density of B,N-graphene under a fuel-cell operating potential (e.g. −0.25 V vs. Ag/AgCl) is much higher and closer to that of Pt/C than that observed for B- or N-graphene (Figure 3b); this result clearly indicates the enhanced synergistic activity of B,N-graphene. The wide current plateau observed for B,N-graphene but not for singly doped graphene (Figure 3b) is considered a strong limiting diffusion current and represents a diffusion-controlled process corresponding to the efficient four-electron-dominated ORR pathway that also occurs on the commercial Pt/C catalyst. We also found that the reversed doping sequence (first with B, then with N) could decrease the electrocatalytic activity of the final product (B,N-graphene-2; see Figure S4d) owing to the formation of a large amount of unfavorable B–C–O groups (see Table S2).

To explore the ORR mechanism and the key electrocatalytic processes on the newly developed catalyst, we carried out a more detailed study of the RDE experiments at different rotating speeds (500–2500 rpm; see Figure S6). As calculated from the slope of Koutecky–Levich (K–L) plots (Figure 3c), the electron-transfer number ($n$) in one ORR process is 3.97 for B,N-graphene, which shows its perfect selectivity (98.5%) for the efficient four-electron-dominated ORR pathway. This excellent electrocatalytic efficiency is much higher than that of B- or N-graphene or the *h*-BN/graphene hybrid and very close to that of the commercial Pt/C catalyst ($n = 3.98$). The technique of the rotating ring–disk electrode (RRDE; see Figure S7) was used to further verify the ORR pathway by monitoring the formation of intermediate peroxide species (e.g. $HO_2^-$ in the alkaline solution) during the ORR process. As shown in Figure 3d, the measured $HO_2^-$ yields were below 10 and 30% for B,N-graphene and *h*-BN/graphene, respectively, over the potential range from −0.4 to −0.8 V. These yields correspond to an electron-transfer number of about 3.8 and 3.5, respectively, and are consistent with the RDE measurements. Both sets of results suggest an enhanced electrocatalytic efficiency of the *h*-BN-free B,N-graphene obtained by the newly developed two-step doping strategy.

Methanol tolerance is an important issue for cathode materials in low-temperature fuel cells and also an obvious shortcoming of Pt-based catalysts. Remarkably, the B,N-graphene catalyst shows perfect ORR selectivity in a methanol-containing environment. Thus, poisoning cross-over effects are avoided (see Figure S8), and B,N-graphene exhibited ideal performance in direct methanol fuel cells. Furthermore, the new catalyst shows higher stability than that of Pt/C with only a small attenuation in its activity during an 85 h testing period (Figure 3e). This result indicates negligible leaching of the B and N dopants during long-term testing in alkaline media. The stability of the catalyst can be ascribed to the stable covalent C–N and C–B bonds in the framework of B,N-graphene.

The synergistic coupling effect in B,N-graphene was quantitatively evaluated in terms of the kinetic limiting current ($J_k$) on the basis of the RDE measurements. The $J_k$ value obtained for B,N-graphene (13.87 mA $cm^{-2}$) surpasses

  

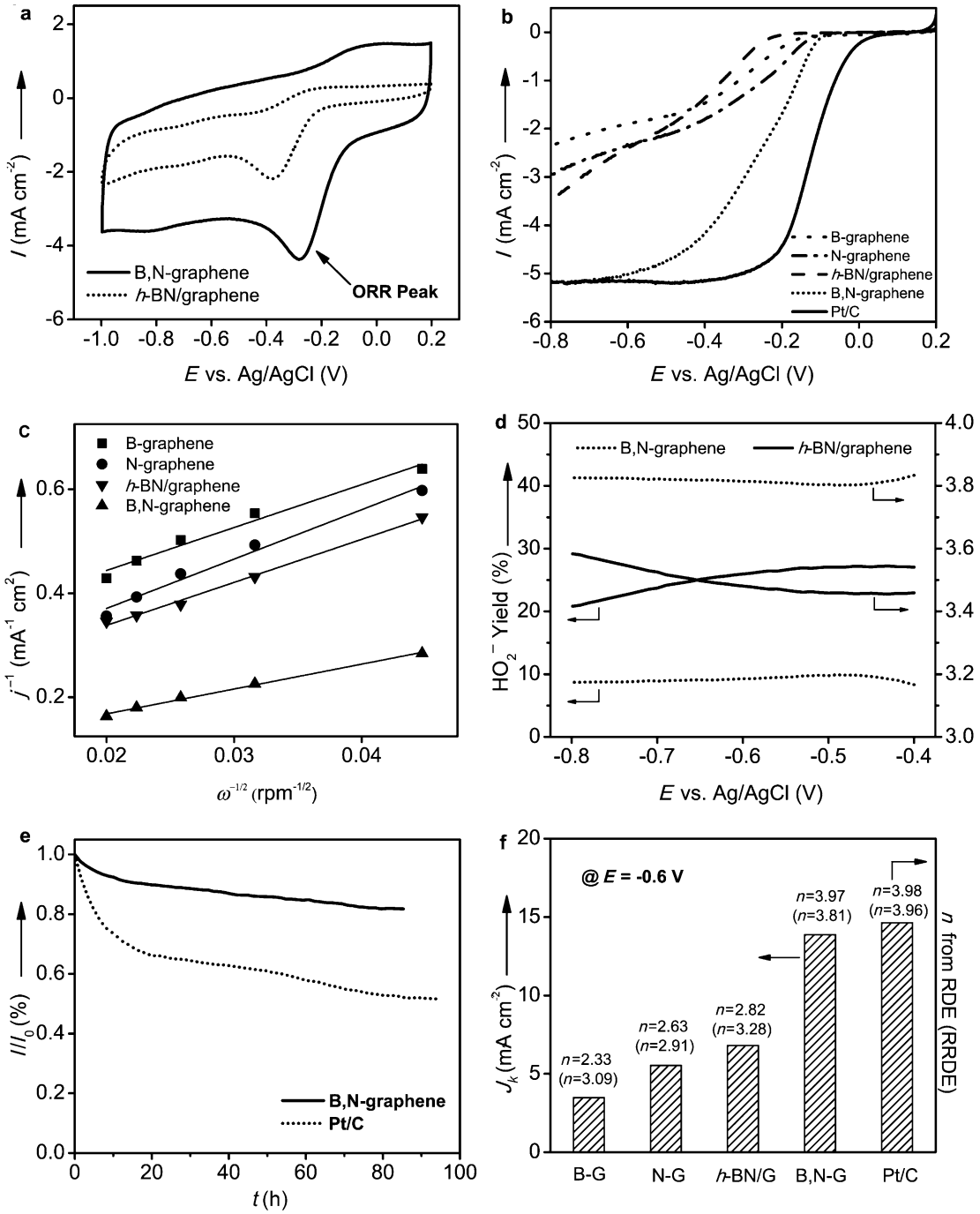


***Figure 3.*** a) Cyclic voltammograms of ORR on B,N-graphene and the *h*-BN/graphene hybrid in an $O_2$-saturated 0.1 M solution of KOH (scan rate: 100 $mV s^{-1}$). b) LSV of various electrocatalysts on a RDE (1500 rpm) in an $O_2$-saturated 0.1 M solution of KOH (scan rate: 10 $mV s^{-1}$). c) K–L plots at −0.6 V for various catalysts on the basis of the RDE data in Figure S6 of the Supporting Information. d) Extent of $HO_2^-$ production and the corresponding electron-transfer number of B,N-graphene and *h*-BN/graphene, as based on the RRDE data in Figure S7 of the Supporting Information. e) Chronoamperometric response of B,N-graphene and Pt/C at −0.3 V in an $O_2$-saturated 0.1 M solution of KOH. f) Summary of the kinetic limiting current density and the electron-transfer number on the basis of the RDE data and the RRDE data (values in parentheses) on various catalysts (G stands for graphene in the *x*-axis labels).

the summed values for singly doped B-graphene (3.48 $mA cm^{-2}$) and N-graphene (5.54 $mA cm^{-2}$; Figure 3 f). Since B,N-graphene had a lower B or N content than the corresponding B- or N-graphene (Figure 1 g; see also Figure S3), these $J_k$ values indicate that the enhanced ORR activity of B,N-graphene, which is close to that of the commercial Pt/C catalyst ($J_k = 14.64\ mA cm^{-2}$), is not a simple superposition of the contributions from B- and N-containing active sites, but may be attributed to a more complicated synergistic effect arising from the coupling interactions between B and N heteroatoms to boost the overall catalytic activity.

We carried out DFT calculations to unveil the microscopic scenario of the aforementioned synergistic effect and electrocatalytic active centers on the newly developed B,N-graphene catalyst (Figure 4; see the Supporting Information for the molecular models and computational details). The energy of $HO_2$ adsorption ($E_{ad}$), which is the rate-determining step of the ORR process,[9] on various catalyst models was used as the criterion to evaluate the ORR activity of each catalyst.[10a,d] The adsorption pattern on each model was obtained by optimizing a set of tentative starting geometries identified by the analysis of charge- and spin-density distribution. As shown in Figure 4a, the active sites for $HO_2$ adsorption in B-graphene are B atoms, and those in N-graphene are C atoms that are next to N atoms. Specifically in the case of N-graphene, a twofold-coordinated pyridinic N dopant at the edge of the cluster has a tendency to suppress the ORR activity; only a graphitic N atom that is far from the graphene edge can induce $HO_2$ adsorption at an adjacent C atom, in agreement with previous experimental and theoretical studies.[10b,c]

For dual-doped B,N-graphene, a higher $E_{ad}$ value than those observed for singly doped B- and N-graphene (Figure 4a) was identified, which suggests its enhanced ORR activity and thereby supports the experimental electrochemical results. As in B-graphene, the ORR active sites of all B,N-graphene models are the threefold-coordinated B dopant owing to its strong electron-donor ability (Figure 4b). Interestingly, only the previously identified inactive pyridinic N atom can boost $HO_2$ adsorption on the active B dopant, whereas graphitic N decreases the activity of B, as shown by the lower adsorption energies (Figure 4c). These results indicate that the various N types that interact with B have very different functions. Furthermore, the transition of the pyridinic N group from "inactive" in N-graphene to "active" after B incorporation can ensure a better activity of B,N-graphene owing to its higher content than that of the graphitic N group in the final product (2.03 atom% vs. 0.9 atom%, as based on experimental data).

The DFT calculations can also provide new insight into the coupling interaction between pyridinic N and B to reveal the origin of the synergistic effect: in a B–C–N heteroring, the 2p orbital of the C atom that is located between the N and B dopants is first polarized by N, which is then able to donate extra electrons to an adjacent B atom. Consequently, the electron occupancy of the 2p orbital of this "activated" B atom is increased to facilitate its adsorption of and bonding with $HO_2$. Thus, this charge-transfer process induces a synergistic coupling effect between N and B dopants, in which N has the role of an electron-withdrawing group to indirectly activate B and thus make the latter an active site to enhance

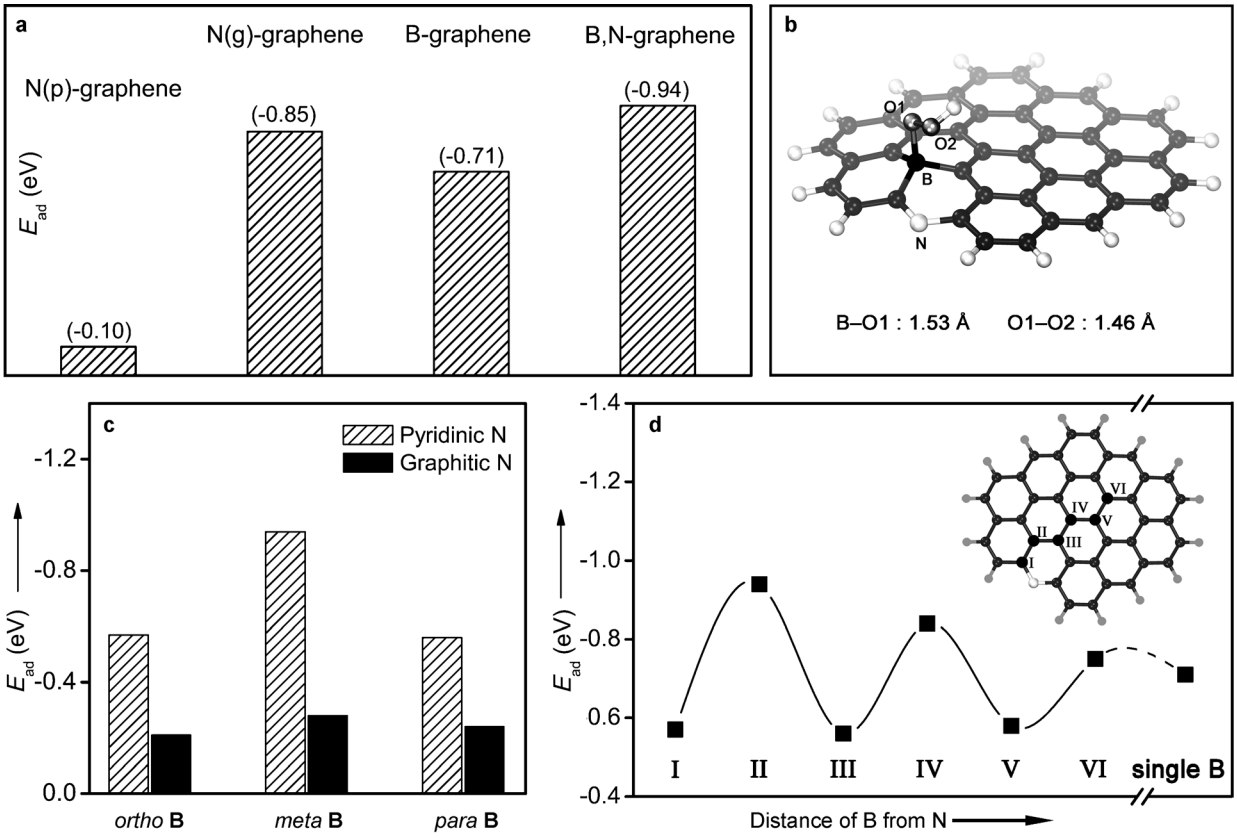


***Figure 4.*** a) Energies of $HO_2$ adsorption ($E_{ad}$) on N- and/or B-doped graphene. N(p) and N(g) indicate pyridinic and graphitic N bonding, respectively. b) Optimized configuration of $HO_2$ adsorbed on B,N-graphene. c) $E_{ad}$ on various B,N-graphene models with pyridinic or graphitic N groups. d) $E_{ad}$ on various B,N-graphene models with B active sites as a function of the distance to a pyridinic N atom (sites I–VI as marked in inset). B-graphene with a single B atom was considered as a reference with an infinitely large distance. Please refer to Figures S11–S14 in the Supporting Information for detailed molecular structures and adsorption configurations.

  

the ORR activity. Among various B–C–N functional configurations in a heteroring, a B atom *meta* to a pyridinic N atom shows the highest $E_{ad}$ value, whereas an *ortho* B atom directly bonded to N (both pyridinic and graphitic forms) as BN has the lowest activity owing to the lack of the C bridge. This result agrees well with the experimental data and theoretically verifies the great effectiveness of the newly developed two-step doping strategy. Furthermore, the strength of the synergistic effect decreases gradually as the distance between the B and pyridinic N dopants increases (Figure 4 d). Thus, the latter dopant is a critical factor for this synergistic effect.

In summary, we have incorporated N and B sequentially into selected sites of the graphene domain to induce an enhanced synergistic coupling effect that facilitates the electrocatalytic ORR. The resultant B,N-graphene exhibited much improved electrochemical performance as compared to that of singly doped graphene and the hybrid electrodes synthesized in one step. Although the onset potential and activity of B,N-graphene are still not as good as those of commercial Pt/C, its good electrocatalytic efficiency, more reliable stability, and relatively low cost make B,N-graphene a promising candidate for the next generation of cost-effective ORR electrocatalysts, particularly for direct methanol fuel cells. Both experimental and theoretical results suggest a feasible molecular design and synthesis strategy towards the development of advanced graphene-based catalysts for energy-conversion technologies.

Received: November 29, 2012
Published online: January 22, 2013

**Keywords:** doping · dual-doped graphene · metal-free catalysis · oxygen reduction · synergistic effects

[1] a) D. S. Su, J. Zhang, B. Frank, A. Thomas, X. Wang, J. Paraknowitsch, R. Schlögl, *ChemSusChem* **2010**, *3*, 169; b) J. Zhang, X. Liu, R. Blume, A. Zhang, R. Schlögl, D. S. Su, *Science* **2008**, *322*, 73; c) K. Gong, F. Du, Z. Xia, M. Durstock, L. Dai, *Science* **2009**, *323*, 760; d) X. Wang, K. Maeda, A. Thomas, K. Takanabe, G. Xin, J. M. Carlsson, K. Domen, M. Antonietti, *Nat. Mater.* **2009**, *8*, 76.

[2] a) Y. Zheng, Y. Jiao, Y. Jin, M. Jaroniec, S. Z. Qiao, *Small* **2012**, *8*, 3550; b) Y. Zheng, Y. Jiao, J. Chen, J. Liu, J. Liang, A. Du, W. Zhang, Z. Zhu, S. C. Smith, M. Jaroniec, G. Q. Lu, S. Z. Qiao, *J. Am. Chem. Soc.* **2011**, *133*, 20116; c) J. Liang, Y. Zheng, J. Chen, J. Liu, D. Hulicova-Jurcakova, M. Jaroniec, S. Z. Qiao, *Angew. Chem.* **2012**, *124*, 3958; *Angew. Chem. Int. Ed.* **2012**, *51*, 3892; d) R. Liu, D. Wu, X. Feng, K. Müllen, *Angew. Chem.* **2010**, *122*, 2619; *Angew. Chem. Int. Ed.* **2010**, *49*, 2565; e) L. Lai, J. R. Potts, D. Zhan, L. Wang, C. K. Poh, C. Tang, H. Gong, Z. Shen, J. Lin, R. S. Ruoff, *Energy Environ. Sci.* **2012**, *5*, 7936; f) S. Guo, S. Zhang, Li. Wu, S. Sun, *Angew. Chem.* **2012**, *124*, 11940; *Angew. Chem. Int. Ed.* **2012**, *51*, 11770.

[3] a) L. Qu, Y. Liu, J. Baek, L. Dai, *ACS Nano* **2010**, *4*, 1321; b) S. Yang, X. L. Feng, X. C. Wang, K. Mullen, *Angew. Chem.* **2011**, *123*, 5451; *Angew. Chem. Int. Ed.* **2011**, *50*, 5339; c) Z. Sheng, H. Gao, W. Bao, F. Wang, X. Xia, *J. Mater. Chem.* **2012**, *22*, 390; d) Z. Liu, F. Peng, H. Wang, H. Yu, W. Zheng, J. Yang, *Angew. Chem.* **2011**, *123*, 3315; *Angew. Chem. Int. Ed.* **2011**, *50*, 3257; e) Z. Yao, H. Nie, Z. Yang, X. Zhou, Z. Liu, S. Huang, *Chem. Commun.* **2012**, *48*, 1027; f) Z. Yang, Z. Yao, G. Li, G. Fang, H. Nie, Z. Liu, X. Zhou, X. Chen, S. Huang, *ACS Nano* **2012**, *6*, 205.

[4] a) S. Wang, E. Iyyamperumal, A. Roy, Y. Xue, D. Yu, L. Dai, *Angew. Chem.* **2011**, *123*, 11960; *Angew. Chem. Int. Ed.* **2011**, *50*, 11756; b) S. Wang, L. Zhang, Z. Xia, A. Roy, D. W. Chang, J. B. Baek, L. Dai, *Angew. Chem.* **2012**, *124*, 4285; *Angew. Chem. Int. Ed.* **2012**, *51*, 4209.

[5] a) J. Liang, Y. Jiao, M. Jaroniec, S. Z. Qiao, *Angew. Chem.* **2012**, *124*, 11664; *Angew. Chem. Int. Ed.* **2012**, *51*, 11496; b) S. Yang, L. Zhi, K. Tang, X. Feng, J. Maier, K. Müllen, *Adv. Funct. Mater.* **2012**, *22*, 3634; c) Z.-S. Wu, A. Winter, L. Chen, Y. Sun, A. Turchanin, X. Feng, K. Müllen, *Adv. Mater.* **2012**, *24*, 5130.

[6] a) T. Lin, C. Su, X. Zhang, W. Zhang, Y. Lee, C. Chu, H. Lin, M. Chang, F. Chen, L. Li, *Small* **2012**, *8*, 1384; b) L. Ci, L. Song, C. Jin, D. Jariwala, D. Wu, Y. Li, A. Srivastava, Z. F. Wang, K. Storr, L. Balicas, F. Liu, P. M. Ajayan, *Nat. Mater.* **2010**, *9*, 430; c) W. Wang, X. Bai, K. Liu, Z. Xu, D. Golberg, E. Wang, *J. Am. Chem. Soc.* **2006**, *128*, 6530; d) X. Yang, L. Liu, M. Wu, W. Wang, X. Bai, E. Wang, *J. Am. Chem. Soc.* **2011**, *133*, 13216.

[7] L. Song, Z. Liu, A. L. M. Reddy, N. T. Narayanan, J. Taha-Tijerina, G. Peng, J. Lou, R. Vajtai, P. Ajayan, *Adv. Mater.* **2012**, *24*, 4878.

[8] E. Raymundo-Piñero, D. Cazorla-Amorós, A. Linares-Solano, J. Find, U. Wild, R. Schlögl, *Carbon* **2002**, *40*, 597.

[9] M. R. Tarasevich, A. Sadkowski, E. Yeager, *Comprehensive Treatise of Electrochemistry*, *Vol. 7*, Plenum, New York, **1983**.

[10] a) L. Zhang, Z. Xia, *J. Phys. Chem. C* **2011**, *115*, 11170; b) R. A. Sidik, A. B. Anderson, N. P. Subramanian, S. P. Kumaragura, B. N. Popov, *J. Phys. Chem. B* **2006**, *110*, 1787; c) S. Huang, K. Terakura, T. Ozaki, T. Ikeda, M. Boero, M. Oshima, J. Ozaki, S. Miyata, *Phys. Rev. B* **2009**, *80*, 235410; d) J. K. Nørskov, J. Rossmeisl, A. Logadottir, L. Lindqvist, J. R. Kitchin, T. Bligaard, H. Jonsson, *J. Phys. Chem. B* **2004**, *108*, 17886.